JOURNAL OF SOLID STATE CHEMISTRY 76, 355–367 (1988)

Influence of Chromium on the Oxidation Kinetics of Annealing Spinels $(Fe^{2+}Al^{3+}_{2-x}Cr^{3+}_x)O^{2-}_4$

B. GILLOT

Laboratoire de Recherches sur la Réactivité des Solides associé au CNRS, Faculté des Sciences Mirande, B.P. 138, 21004 Dijon Cedex, France

A. ROUSSET

Laboratoire de Chimie des Matériaux Inorganiques, LOE–CNRS, 29, rue Jeanne Marvig, 31055 Toulouse Cedex, France

AND F. CHASSAGNEUX

Laboratoire de Chimie Minérale III, Universite Claude Bernard, 43 boulevard du 11 novembre 1918, 69622 Villeurbanne Cedex, France

Received January 29, 1988; in revised form May 16, 1988

The oxidation of annealing spinels $(Fe^{2+}Al^{3+}_{2-x}Cr^{3+}_x)O^{2-}_4$ in metastable deficient spinels γ-$(Fe^{3+}_{8/9}Al^{3+}_{8/9(2-x)}Cr^{3+}_{8x/9}\square_{1/3})O^{2-}_4$ at temperatures in the range 350–450°C and over the pressure range 50–10^4 Pa has been studied with special emphasis on the effect on chromium content. When particle size is increased by annealing crystals of more than approximately 200 to 500 nm, the kinetic curves are sigmoidal, but only for spinels with high chromium content. Although the kinetic results are well interpreted by the Prout–Tompkins model (E. G. Prout and F. C. Tompkins, *Trans. Faraday Soc.* **40,** 488 (1944)), the morphological observations and the X-ray diffraction data suggest an autocatalytic process. © 1988 Academic Press, Inc.

Introduction

As part of our studies on oxidation kinetics of ferrous spinels, we investigated the influence of chromium content and annealing temperature on morphology and kinetic behavior in oxygen of $(Fe^{2+}Al^{3+}_{2-x}Cr^{3+}_x)O^{2-}_4$ $(0 < x < 2)$ type spinels. Previous studies (*1*) have shown that for samples prepared near 600°C, with crystallite sizes below 300 nm, the oxidation kinetics are controlled by diffusion, under variable conditions, of vacancies generated at the solid–gas interface according to the reaction in the Kröger and Vinck notation (*2*):

$$\tfrac{1}{2}O_{2(g)} + 2Fe_{Fe_{II(t)}} \rightleftarrows \tfrac{1}{4}V''_{Fe_{II(t)}} + \tfrac{1}{2}V'''_{(Al,Cr)_{III(0)}} + \ldots 2Fe^{\cdot}_{Fe_{II(t)}} + O_0. \quad (1)$$

Under these conditions, for spherical particles, the experimental curves can be described by:

$$W_t/W_\infty = \alpha = 1 - (6/\pi^2)\sum_{n=1}^{\infty}(1/n^2)e^{-n^2kt}, \quad (2)$$

with $k = \pi^2\tilde{D}/r^2$, where $\tilde{D}$ is the chemical

0022-4596/88 $3.00

Copyright © 1988 by Academic Press, Inc.
All rights of reproduction in any form reserved.

diffusion coefficient, r the mean grain radius, and $W_t/W_\infty = \alpha$, the fractional mass change. This oxidation mechanism does not require the formation of a protective layer over the initial spine; the crystal lattice is not disrupted, and the transformation does not involve nucleation of a new solid phase. Thus, the oxidation reaction is topotactic, with preservation of the oxygen lattice; it thus yields γ-cation deficient spinels.

However, several factors affect this diffusion: the crystallite size (*3*), the extent of trivalent substitutions (*4*), and the nature of the substituent. Thus, the activation energy of the oxidation reaction, as well as the oxidation temperature, varies considerably, depending on the above factors, described later. Thus, for oxidation of pure magnetite over the range 200–400°C, the activation energy rises from 99 to 146 kJ $mole^{-1}$ as the grain size increases from 60 to 400 nm (*3*). For this latter case, the oxidized product contains tiny amounts (3–4%) of the rhombohedral α-phase, although the reaction always proceeds by diffusion of the iron ions. X-ray diffraction patterns taken at successive stages of oxidation showed shifts of the diffraction lines toward lower d-values, with a contraction of the unit cell as magnetite changed to maghemite (*3*). Electron micrographs revealed that the morphology of maghemite particles was very similar to that of the initial particle. In particular, any fragmentation of the crystal occurs owing to lattice parameter changes.

The effect of trivalent cations (Al^{3+}, Cr^{3+}) on the oxidation characteristics is more complex: in preliminary kinetic and morphologic investigations we detected the strong influence of the chromium content on the kinetics along with the effect of crystallite size which is influenced by annealing.

In the present study we investigate more thoroughly the changes in morphology, lattice parameter, and kinetics which accompany the low temperature oxidation (350–470°C) of the solid solutions $FeAl_2O_4$–$FeCr_2O_4$ as prepared via a metal–organic precursor method. The annealing schedule subsequent to the thermal decomposition of the precursors permits one to regulate the average dimensions of the crystallites.

Experimental Procedure

Preparative conditions for spinel of the $(Fe^{2+}Al^{3+}_{2-x}Cr^{3+}_x)O^{2-}_4$-type ($0 < x < 2$) were provided by Rousset (*5*). These phases are obtained by reducing at 700°C in H_2–H_2O atmosphere a rhombohedral solid solution $(Fe^{3+}_{1/3}Cr^{3+}_xAl^{3+}_y)_2O^{2-}_3$ prepared from the decomposition in air of the organic salts $(NH_4)_3(Fe_{1/3}Al_yCr_x)(C_2O_4)_3 \cdot 3H_2O$ with $(x + y) = \frac{2}{3}$. For samples obtained at 700°C, the particle size is in the range 30–60 nm (Table I, group A). When the same samples are annealed under vacuum at higher temperatures, the particle size increases and varies with the substitution extent and with temperature (Table I, groups B, C, D). Table I also shows that only samples with high chromium content appreciably increase in size with annealing temperature. The size varies less with annealing for compounds delayed with aluminum; the particles do not exceed 80 nm at 1100°C.

Transmission electron microscopic studies of samples annealed at 1100°C showed that the aluminate (Fig. 1) consists of small hexagonal particles roughly 60–80 nm in diameter. Spinels with high chromium content (Figs. 2 and 3) essentially exhibit projection with six or fewer edges, corresponding to {100} and {111} faces which are most common, with diameters of several hundred nanometers. A few of the crystals are thin hexagonal platelets (Fig. 4). The d-spacings in Fig. 5a of 0.470 and 0.250 nm in $FeCr_{1.6}Al_{0.4}O_4$ correspond to the (111) and (311) planes of the spinel structure. Samples whose composition is close to that of iron chromite ($x > 1.6$) display grain boundaries (Fig. 5b); here, the crystallite size determined from the specific area is larger

TABLE I

SOME CHARACTERISTICS OF THE $(Fe^{2+}Al^{3+}_{2-x}Cr^{3+}_{x})O^{2-}_{4}$ SPINELS

Samples	Preparation (Group A) and annealing temperature (groups B, C, D) (°C)	Specific area (m^2/g)	Crystallite mean size (nm)		Lattice parameter (nm)
			Specific area	Electron microscopy	
$x = 0$	A_0 700	45	31		0.8159
	B_0 900	33	50	45	
	C_0 1100	21	80	75	
$x = 1.2$	$A_{1.2}$ 700	30	35		0.8300
	$B_{1.2}$ 900	17	85		
	$C_{1.2}$ 1100	11	110		
$x = 1.6$	$A_{1.6}$ 700	23	37	30	0.8340
	$B_{1.6}$ 900	5	130	90	
	$C_{1.6}$ 1100	3.7	200	140	
	$D_{1.6}$ 1200	1.7	430		
$x = 2$	A_2 700	22	80		0.8378
	B_2 900	3.5	200	150	
	C_2 1100	1.7	450	340	
	D_2 1200	1.1	490	360	

Note. Group A: Samples prepared at 700°C. Groups B, C, and D: Samples annealed at 900, 1100, and 1200°C, respectively.

than that determined from the micrographs (Table I).

The oxidation was performed on a microbalance Setaram MTB 10-8, with 5 mg of powder uniformly spread at the bottom of the scoop so that it oxidizes as independent particles. The total oxidation is determined from the experimental weight gain. The partial oxidations used for determining the lattice parameter and morphological obser-

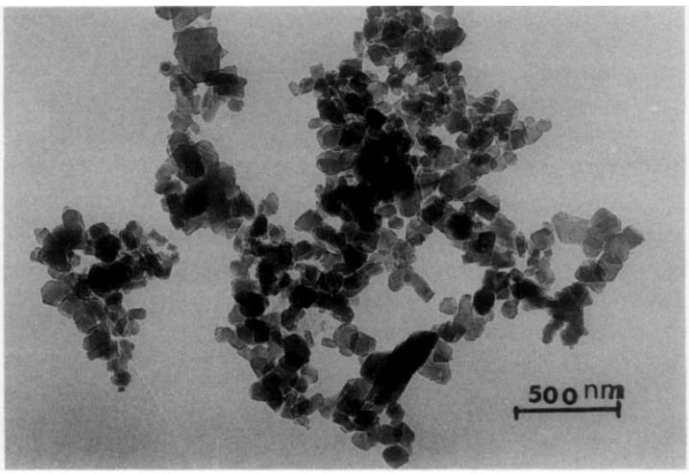

FIG. 1. Electron micrograph of initial $FeAl_2O_4$ particles annealed at 1100°C.

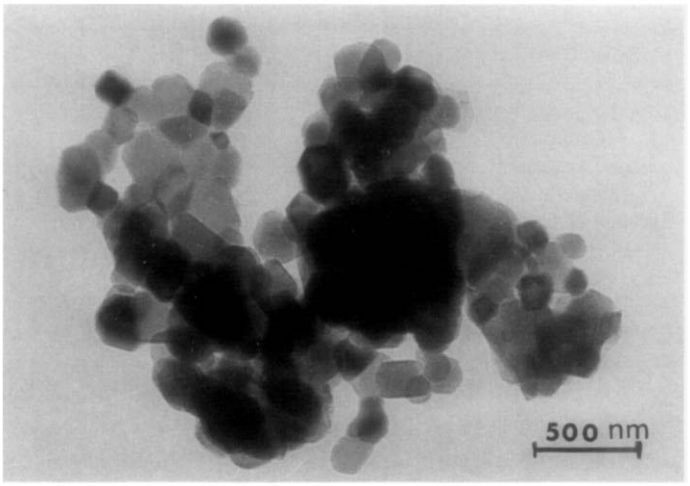

FIG. 2. Electron micrograph of initial $FeAl_{0.4}Cr_{1.6}O_4$ particles annealed at 1100°C.

vations were obtained by interrupting the reaction. The conversion rate α is determined from the ratio of partial oxidation weight gain to completed oxidation weight gain.

Results

1. Kinetic Study

The oxidation kinetics relative to the extent of chromium substitution and to the annealing temperature are shown in Figs. 6, 7, and 8. The kinetic curves (Fig. 6) for similar annealing temperatures (e.g., 1100°C) with different chromium extent become sigmoidal when composition approaches that of iron chromite. For a similar degree of substitution (Figs. 7 and 8) the initial curves parabolic for samples prepared at 700°C (group A) become sigmoidal when the same samples are annealed at different temperatures. As already shown in Ref. (*3*), the ki-

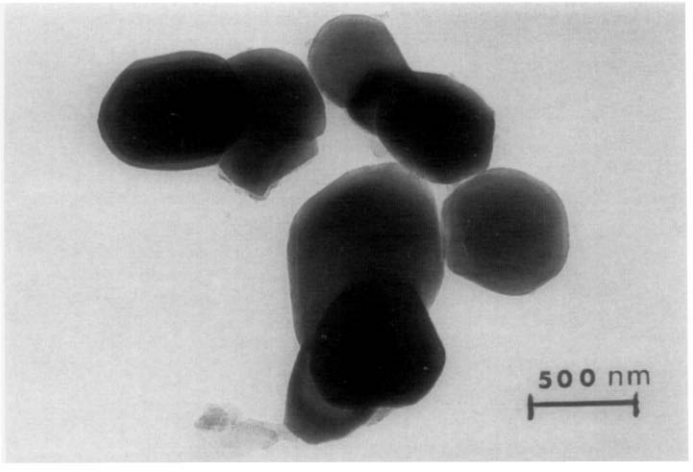

FIG. 3. Electron micrograph of initial $FeCr_2O_4$ particles annealed at 1100°C.

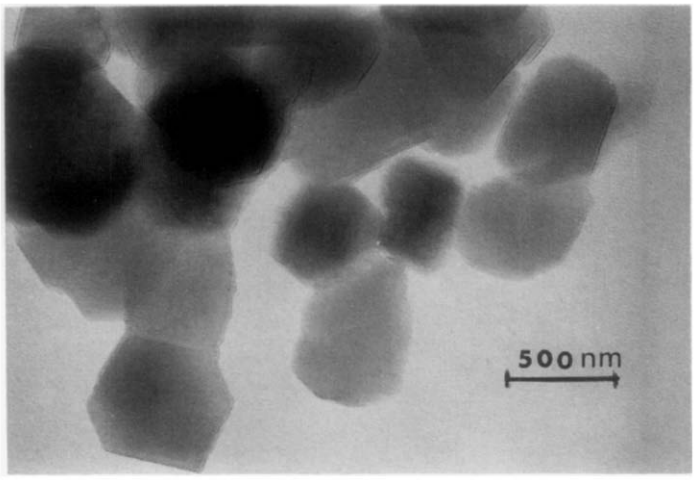

FIG. 4. Thin hexagonal platelets of $FeCr_2O_4$.

netics of oxidation of Fe_3O_4 indicate that the reaction is independent of annealing temperature and is solely governed by bulk ionic diffusion.

Effect of temperature. For the two compositions $x = 1.6$ and $x = 2$ and for different annealing temperatures, the isothermal curves $\alpha = f(t)$ (Fig. 9) are sigmoidal, with a maximum rate for $\alpha_{i(1.6)} = 0.40$ and $\alpha_{i(2)} = 0.50$, where α_i represents the α value at which the rate $d\alpha/dt$ is maximum. In both cases they can be superimposed for $0.1 < \alpha$

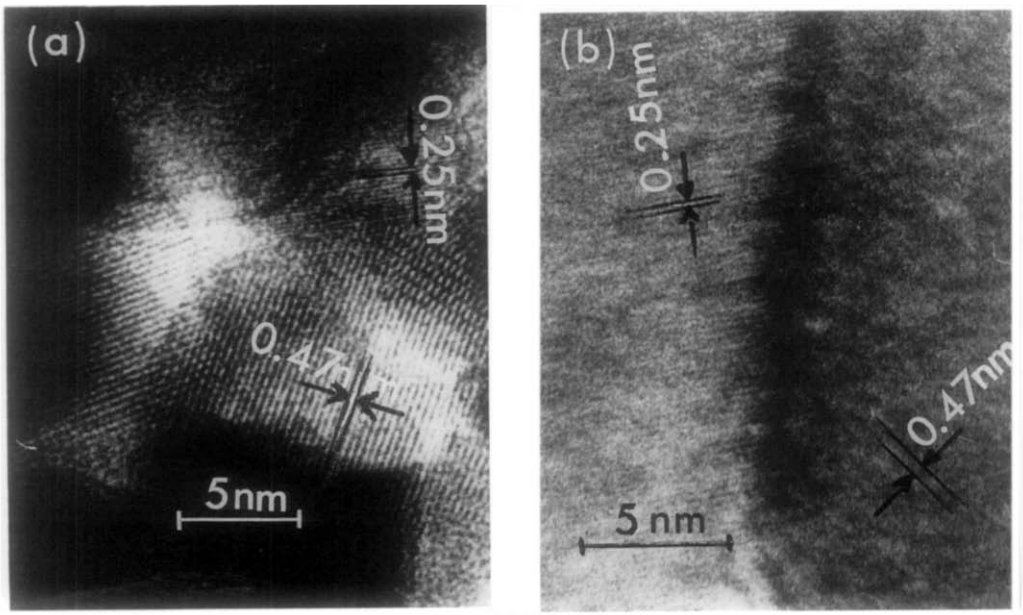

FIG. 5. Lattice images: (a) of initial $FeCr_2O_4$; (b) grain boundary.

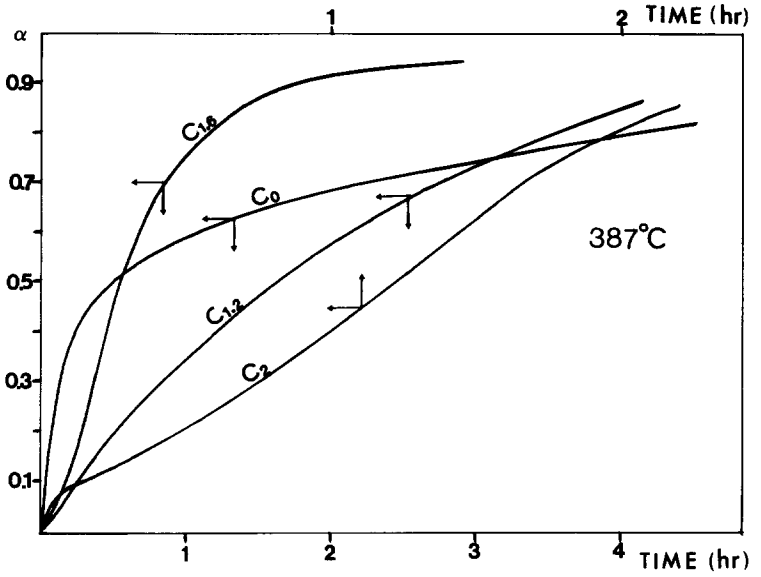

FIG. 6. $\alpha = f(t)$ curves for different chromium content and for an annealing temperature of 1100°C.

< 0.9 for samples of composition $x = 1.6$ and $0.2 < \alpha < 0.85$ for samples with $x = 2$. A master run roughly in the middle of the series was chosen and a factor A found for each run such that multiplication of the time scale of the run by A would superimpose it onto the master run curve. The activation energy may then be calculated by plotting $\log A$ vs $1/T$ (E_1) or by plotting the logarithm of the instantaneous rate $v_i = d\alpha/$

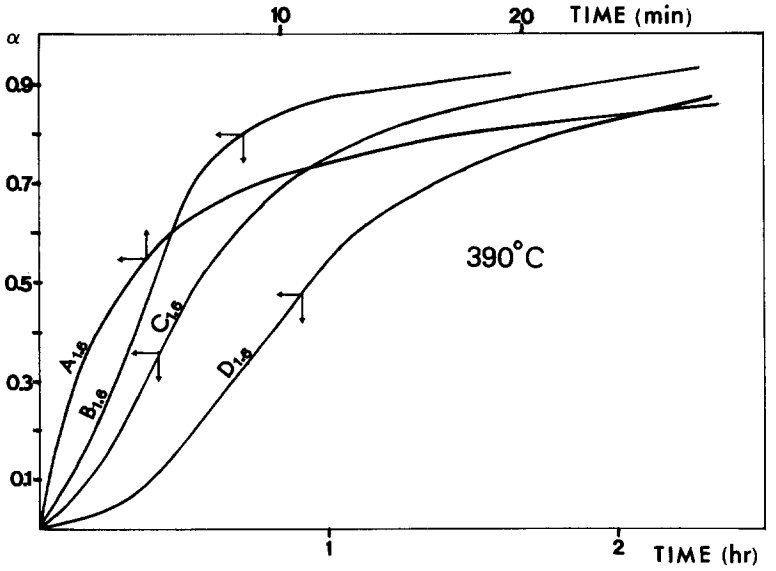

FIG. 7. $\alpha = f(t)$ curves for different annealing temperatures and for $x = 1.60$.

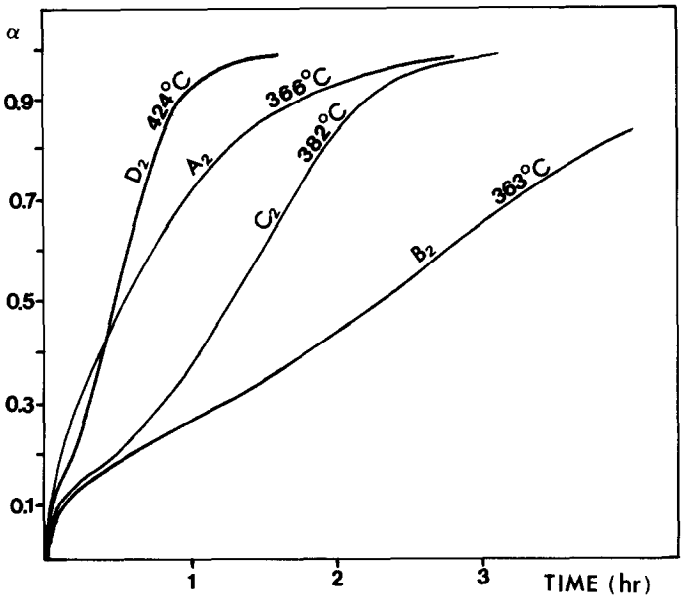

FIG. 8. $\alpha = f(t)$ curves for different annealing temperatures and for $x = 2$.

dt vs $1/T$ (E_2) at different constant values of α. The activation energy obtained for different annealing temperatures are listed in Table II.

Effect of pressure. The sigmoidal shape is preserved (Figs. 10 and 11) and the curves can be superimposed. Plots of log A or log v_i vs log P yield families of parallel

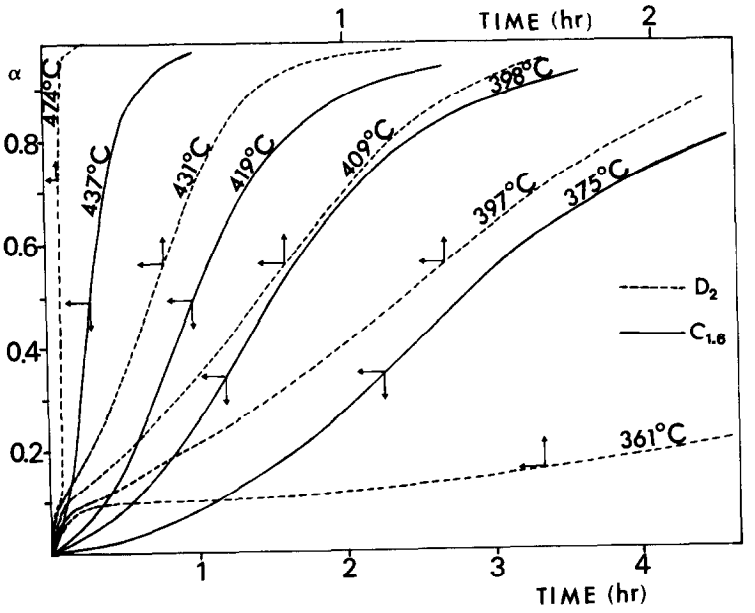

FIG. 9. $\alpha = f(t)$ curves for $x = 1.60$ and $x = 2$; temperature law. $P_{O_2} = 10^3$ Pa.

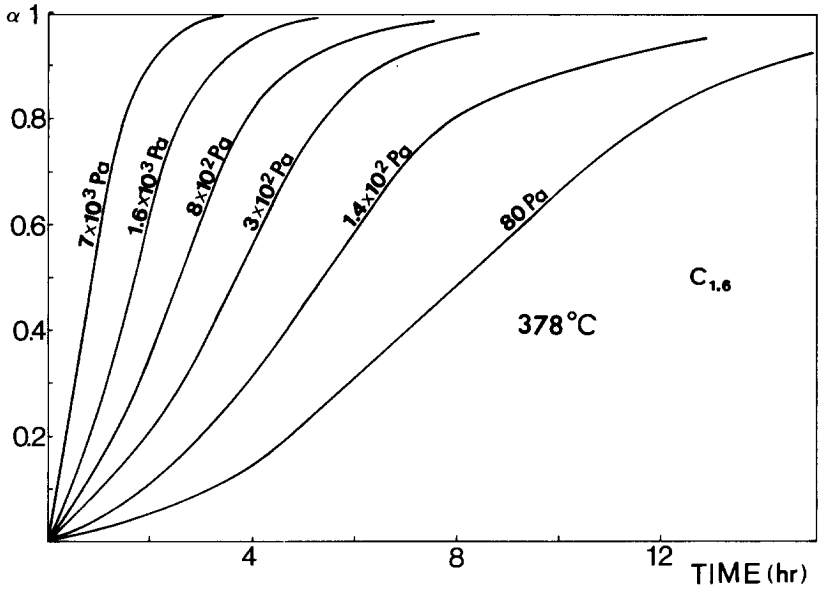

FIG. 10. $\alpha = f(t)$ curves for $x = 1.60$; pressure law. $T = 378°C$.

straight lines whose slopes n_1 and n_2 are listed in Table II. The relation of the reaction rate to pressure is thus written $v = kP^n$. For the sample of composition $x = 2$, where a separate initial period is observed over a range $0 < \alpha < 0.20$, Delmon's "constant interface method" (*6*) has been used (Fig. 11) in order to separate the different

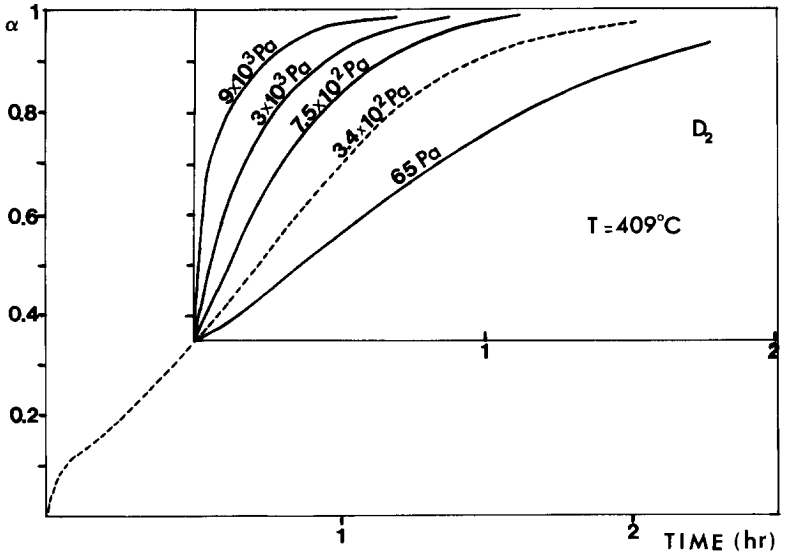

FIG. 11. $\alpha = f(t)$ curves for $x = 2$ (Delmon's (*6*) method); pressure law. $T = 409°C$.

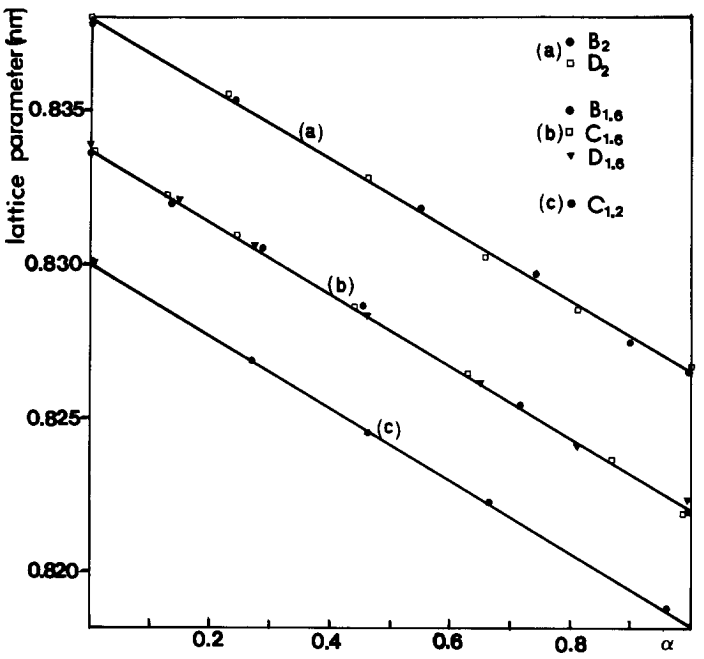

FIG. 12. Evolution of lattice parameter versus the fractional mass change α for different compositions and different annealing temperatures.

stages of the reaction, i.e., the interface formation (initial period of nucleation) and the progress of the interfacial reaction.

2. *Crystallographic Study and Morphological Observations*

Oxidation was followed by X-ray analysis for various conversion ratios α. In all cases the spinel structure was preserved; only a steady decrease in lattice parameter with increasing α is observed (Fig. 12) consistent with the smaller ionic radius of Fe^{3+} (0.065 nm) as compared to Fe^{2+} (0.074 nm), according to structural formula (*1*):

$$(Fe^{3+}_{8/9}Al^{3+}_{(2-x)8/9}Cr^{3+}_{8x/9}\square_{1/3})O^{2-}_4.$$

Electron microscopy showed that the morphology of partially or totally oxidized particles was similar to that of initial particles from which they were obtained (Figs. 13, 14, and 15). In particular, no fragmentation appears after oxidation. In chromite particles, the hexagon angle which was very smooth before oxidation becomes sharp and faceted during the oxidation reaction (Figs. 14 and 15).

TABLE II

EXPERIMENTAL KINETIC RESULTS

	Energy in kJ mole^{-1}				Pressure law (n values)			
Samples	E_1	E_2	E_3	E_4	n_1	n_2	n_3	n_4
$B_{1.6}$	119	117	116	117				
$C_{1.6}$	124	126	124	126	0.45	0.44	0.44	0.47
$D_{1.6}$	128	130	129	129				
B_2	110	111	110	109				
C_2	115	115	116	115	0.51	0.49	0.53	0.48
D_2	133	136	135	134				

Discussion and Conclusion

The affine character of the curves indicates that the states traversed by the system during the reaction are dependent on intensive variables such as temperature and

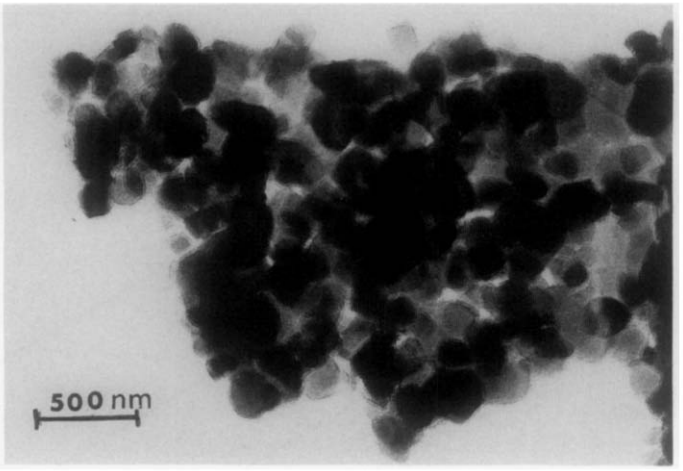

FIG. 13. Electron micrograph of oxidized (α = 1) $FeAl_{0.4}Cr_{1.6}O_4$ particles annealed at 1100°C.

pressure. The rate equation for the process can be written in terms of separated variables as

$$v = d\alpha/dt = K_p K_T P^n e^{-E/kT} f(\alpha), \quad (3)$$

where $f(\alpha)$ depends on the mechanism controlling the reaction. At constant temperature and pressure the shape of the curves is determined only by $f(\alpha)$. We find a very good linear representation of the sigmoidal curves (Fig. 16) if $f(\alpha)$ is an equation of type:

$$f(\alpha) = \log\left(\alpha \Big/ \left(1 - \frac{\alpha}{2\alpha_i}\right)\right) = k_1 t + C^{te}, \quad (4)$$

which is the integrated form of the Prout–Tompkins equation (7). The rate for the

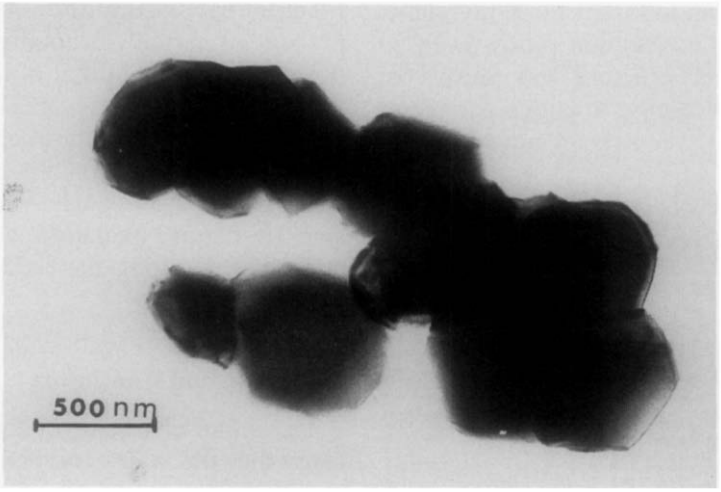

FIG. 14. Electron micrograph of partially oxidized (α = 0.37) $FeCr_2O_4$ particles annealed at 1100°C.

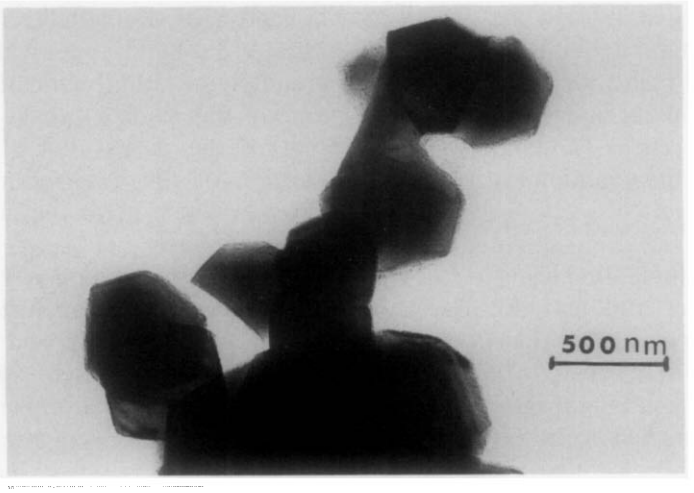

FIG. 15. Electron micrograph of totally oxidized ($\alpha = 1$) $FeCr_2O_4$ particles annealed at 1100°C.

process can be thus written as:

$$d\alpha/dt = k_1\alpha(1 - \alpha/2\alpha_i) \; . \qquad (5)$$

From the temperature dependence of k_1 (Fig. 16) an apparent activation energy E_3 is deduced for compositions $x = 1.60$ and $x = 2$ (Table II). The values are very close to that calculated from the affinity ratio (Table II). The n_3 values obtained by plotting log v_i ($v_i = d\alpha/dt$) vs log P are also comparable (Table II).

X-ray diffraction results and morphologi-

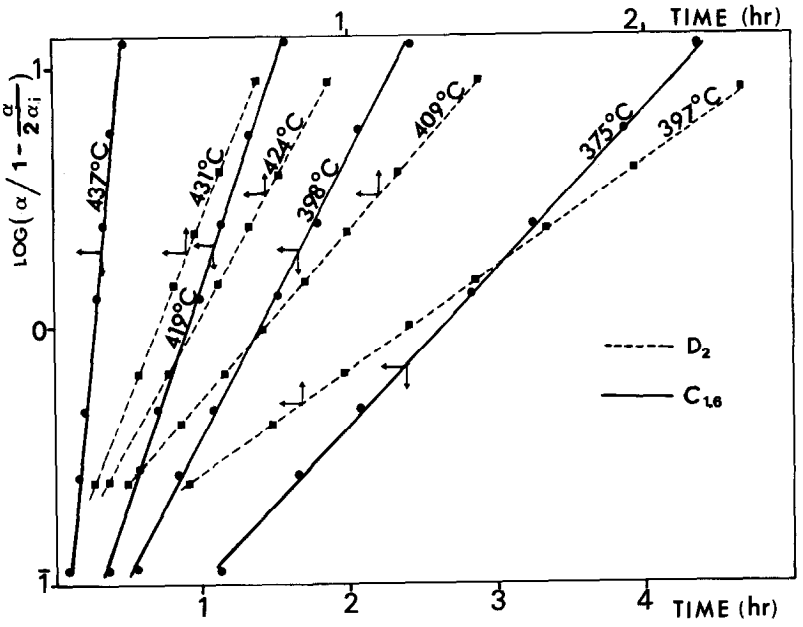

FIG. 16. Conversion as a function of time plotted in terms of Eq. 4.

cal observations show that we must consider an autocatalytic process rather than a branched chain nucleation mechanism, i.e., the Prout–Tompkins model (*7*). In this case the kinetic analysis of TG data also can be represented by the equation (*8*)

$$d\alpha/dt = k'\alpha(1 - \alpha), \qquad (6)$$

which through integration leads to $f(\alpha)$ with $\alpha_i = \frac{1}{2}$. However, this may not always be the case; values of α_i other than 0.5 are also possible. Bond (*9*) in his study on the reduction of CuO (which is autocatalytic) has in fact used a modified form of the Prout–Tompkins equation leading to Eq. (6). The term $\alpha(1 - \alpha)$ is proportional to the effective area of the reaction front (*10*). On the other hand the pressure laws correspond to Freundlich's isotherm, consistent with heterogeneity of the adsorption sites and with an external interfacial reaction as controlling process. Such a reaction would proceed at a constant speed and the global rate would be modulated by the morphological factors according to Eq. (3).

However, at no time does the accelerating period correspond to grain fragmentation; the $\alpha = f(t)$ curves cannot be interpreted for $\alpha < \alpha_i$ by an increase of area of the solid–gas interface owing to the Pilling–Bedworth (*11*) expansion coefficient Δ (here $\sim$1.1) which represents the ratio between the molar volumes of the reaction product and the reactant. A comparison of the XRD patterns from the original and treated samples in oxygen revealed an increase in half-maximum width of X-ray diffraction lines for conversion ratios of $0.1 < \alpha < 0.30$. The accelerating period can be explained by considering the particles to be composed of inner core of an oxidized spinel, with an outer region of partially or totally oxidized spinel, to consist of two phases rather than being a homogeneous solid (*12*). Thus, initially when a grain of $FeCr_2O_4$ is exposed to an oxidizing atmosphere the particles are partially covered by "islands" of cation-deficient spinel rich in iron (i.e., γ-Fe_2O_3 type) which appear preferentially at grain boundaries. As the volume of the oxidized phase is greater than that of the parent $FeCr_2O_4$ (*4*), the expansion of the oxidized regions induces stresses which favor the nucleation of the γ-defect phase.

For higher conversion ratios ($\alpha > \alpha_i$), when the particles are further oxidized, a progressively thicker and more uniform layer of cation-deficient spinel is formed. X-ray diffraction patterns showed no appreciable line broadening compared to initial spinel. It is possible to interpret the kinetic curves by a law of type (*13*):

$$F(\alpha)_{\alpha>\alpha_i} = 1 - (1 - \alpha)^{1/3} = kt. \qquad (7)$$

This can be checked by the linear plots of $F(\alpha)_{\alpha>\alpha_i}$ vs time. The activation energies (E_4) and the n values (n_4) computed from the slopes of these plots are very close to the experimental ones (Table II).

In conclusion, this study shows the importance of morphological data in the kinetic behavior of a gas–solid reaction of type $S_1 + G \rightarrow [S_1 + d]$ where $[S_1 + d]$ expresses the phase enriched in defects. We thus established that the diffusion law usually obtained for spinels prepared at 700°C is replaced by a sigmoidal law for annealing spinels containing large amounts of chromium. However, the monophasic character of the crystal remains. The morphological observations, X-ray analysis, and the oxidation curves suggest that the autocatalytic process may be rate controlling rather than a nucleation process, this being confirmed by the oxygen pressure dependence of the rate law.

References

1. B. GILLOT, F. BOUTON, F. CHASSAGNEUX, AND A. ROUSSET, *Mater. Res. Bull.* **15,** 1 (1980).
2. F. A. KRÖGER AND H. J. VINCK, *in* "Solid State Physics" (F. Seitz and D. Turnbull, Eds.), Academic Press, New York (1956).

3. B. GILLOT, A. ROUSSET, AND G. DUPRE, *J. Solid State Chem.* **25,** 263 (1978).
4. B. GILLOT, J. F. FERRIOT, G. DUPRE, AND A. ROUSSET, *Mater. Res. Bull.* **11,** 843 (1976).
5. F. CHASSAGNEUX AND A. ROUSSET, *J. Solid State Chem.* **16,** 161 (1976).
6. B. DELMON, "Introduction à la cinétique hétérogène," Technip, Paris (1969).
7. E. G. PROUT AND F. C. TOMPKINS, *Trans Faraday Soc.* **40,** 488 (1944).
8. J. DEMIASON AND W. BILLY, *J. Chim. Phys.* **72,** 417 (1975).
9. W. D. BOND, *J. Phys. Chem.* **66,** 1573 (1962).
10. P. BARRET, "Cinétique hétérogène," Gauthier-Villars, Paris (1973).
11. M. B. PILLING AND R. E. BEDWORTH, *J. Inst. Met.* **29,** 529 (1923).
12. J. E. KNOWLES, *J. Magn. Magn. Mater.* **22,** 263 (1981).
13. J. DEMAISON AND W. W. SMELTZER, *J. Electrochim. Soc.* **122,** 354 (1975).